RESEARCH PAPER

Performance comparison of COTS-based hyperspectral imagers using detailed point spread function measurements

Gard Momrak Selnesaunet,[a] Marie Bøe Henriksen [b] and Torbjørn Skauli [a,*]

[a]University of Oslo, Centre for Space Sensors and Systems,
Department of Technology Systems, Kjeller, Norway
[b]Norwegian University of Science and Technology, Center for Autonomous Marine Operations and Systems,
Department of Engineering Cybernetics, Trondheim, Norway

ABSTRACT. Hyperspectral imaging is a rapidly growing field that utilizes a diverse range of camera designs. It has been demonstrated that hyperspectral cameras can be constructed from commercial off-the-shelf (COTS) components, offering the potential for low-cost and widespread use. However, these COTS-based systems may face performance limitations due to optics not being optimized for hyperspectral purposes. Characterizing and comparing the performance of hyperspectral cameras is complex, a challenge recognized by the ongoing development of the IEEE P4001 standard. Specifically, the spatial coregistration among different spectral bands is crucial for the quality and integrity of the recorded spectra in each pixel. The proper evaluation of coregistration and resolution necessitates the measurement of the point spread function for each band. We use measurements of the full 2D sampling point spread function (SPSF) to compare the performance of two hyperspectral imagers (HSIs) built from COTS components: the engineering model of the hyperspectral camera onboard the Hyperspectral Cubesat for Ocean Observation-1 cubesat and an extremely compact HSI developed for drone flights. In addition, the line spread functions across and along the track, keystone distortion, and coregistration errors are derived from the SPSFs. A simplified measurement scheme is also tried and found to provide fair accuracy for the tested cameras. The results highlight the importance of measuring the spatial SPSF for characterizing and comparing different hyperspectral cameras. Results also show that good spectral integrity can be achieved through spatial binning, which of course requires a tradeoff against spatial resolution. Nonetheless, it is evident that such low-cost systems can offer useful capabilities.

1 Introduction

The use of hyperspectral imaging on small platforms such as drones and cubesats is gaining significant attention due to the broad range of potential applications enabled by swarms of drones or constellations of microsatellites. Operating on small platforms imposes significant constraints

---

*Address all correspondence to Torbjørn Skauli, torbjorn.skauli@its.uio.no

on payload size and optical aperture diameter, which in turn restricts spatial resolution due to the diffraction limit. Despite these constraints, hyperspectral imaging can extract extensive spectral information from each pixel, which partially offsets the limitations in spatial resolution. This capability is particularly beneficial in fields such as land use mapping and ecosystem health assessment.

For applications involving many platforms, there will inevitably be a tradeoff between performance and cost. In this context, an interesting option for cost-sensitive applications is the design of Sigernes et al.,[1] which is based on commercial off-the-shelf (COTS) parts, supplemented by some 3D printable parts. This design has been further developed to be used as a cubesat payload in Refs. [2] and [3], although with increased volume, weight, and cost. In this paper, we compare these two generations of COTS-based cameras.

The performance of a hyperspectral camera is multifaceted. The IEEE Standards Association Project 4001 (P4001)[4] is developing a standard for the specification of hyperspectral cameras, which will define more than 40 performance characteristics. In imaging, spatial resolution is a primary indicator of performance. In spectral imaging, the spatial coregistration between bands is an aspect of performance that is less prominent but crucial for the integrity of the spectral signal. Spatial characterization of hyperspectral cameras has typically been done by measuring the line spread function (LSF) in the across- and along-track directions,[5,6] or by imaging a bar chart,[7] to derive the point spread function width and the wavelength-dependent peak shift known as keystone. These metrics are widely reported but do not capture the full range of effects that can degrade the integrity of measured spectra.[8] In this study, we measure the full 2D sampling point spread function (SPSF) of each band (i.e., the distribution of sensitivity in the scene for a given pixel) and derive spatial resolution, keystone distortion, and the full coregistration error from the measured SPSFs. We demonstrate how SPSF measurements provide valuable insights for comparing hyperspectral cameras and discuss aspects of the measurement process. The results quantify the level of performance attainable with a hyperspectral camera built from COTS components. The upcoming P4001 standard defines camera performance characteristics derived from measured SPSFs. This paper builds on previous work[9,10] and extends the limited body of published 2D measurements of SPSF for hyperspectral cameras.

2 Experimental

2.1 Cameras Under Test

The two hyperspectral imagers (HSIs) evaluated in this study, referred to as HSI V4 and HSI V6, are pushbroom imagers constructed from COTS components. These were developed for engineering purposes during the Hyperspectral Cubesat for Ocean Observation 1 (HYPSO-1) project. Detailed information about the design and construction of these instruments can be found in Refs. [1] and [2] for the HSI V4 and HSI V6, respectively. Both cameras share the same basic optical design, featuring a transmissive grating as the dispersive element, a high-precision slit, a collimator lens, and a front lens. The cameras are also equipped with the same focal plane arrays for data capture. However, the optical components differ in size: HSI V4 is equipped with smaller S-mount optics, whereas HSI V6 utilizes larger C-mount optics, allowing it to collect more light than HSI V4. All the optics are objective lenses intended for use with machine vision cameras operating in the visible spectral range. The main characteristics of the instruments are summarized in Table 1.

As the lenses in the cameras are intended for commercial color imaging with broadband illumination, significant deviations from ideality must be expected when they are used in a hyperspectral camera. Notably, the resolution of such lenses is specified in terms of their modulation transfer function (MTF) averaged over the visible spectral range. Behind this average is normally a significant wavelength dependence of image sharpness, as the results below illustrate.
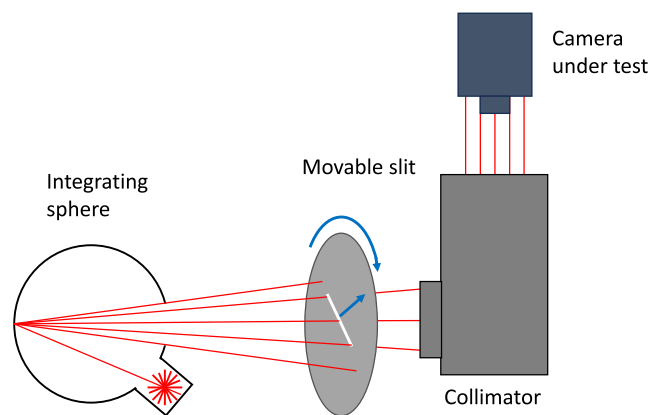
2.2 Measurement Set-Up

Our measurement setup builds on the work presented in Ref. [9]. A preliminary version was reported in Ref. [10]. A schematic representation of the setup is shown in Fig. 1. The measurement technique is based on a line source scanned across a pixel while recording data, producing a 1D

Table 1 Specifications of the HSI V4 and HSI V6.

Specification	HSI V4	HSI V6
Camera sensor	Sony IMX174	Sony IMX174
Shutter	Global	Global
Number of effective pixels	$1936\,(H) \times 1216\,(V)$	$1936\,(H) \times 1216\,(V)$
Pixel size	$5.86\ \mu$m	$5.86\ \mu$m
Focal length	17.5 mm	17.526 mm
Slit length	3 mm	7 mm
Slit width	$25\ \mu$m	$50\ \mu$m
FOV along track	0.089 deg	0.057 deg
FOV across track	10.712 deg	8.008 deg
Optical magnification	1.2	1
Grating	600 lines/mm	300 lines/mm
Theoretical spectral FWHM	1.4 nm	3.3 nm
Design center wavelength	552.5 nm	600 nm
Design spectral range[a]	400 to 800 nm	400 to 800 nm
Average spectral sampling interval	0.399 nm per pixel	0.396 nm per pixel
Size	$125 \times 35 \times 35$ mm^3	$200 \times 65 \times 65$ mm^3
Weight	157 g	650 g

[a]Both instruments are designed for the 400- to 800-nm range and are expected to be used within this range only, unless corrections are applied to the data.

Fig. 1 Schematic drawing of the SPSF measurement setup

LSF. By scanning in different directions, it is possible to reconstruct the full 2D shape of the SPSF in each band for the set of pixels covered by the scan.

The set-up consists of a collimator (Inframet CDT 11100HR off-axis reflective collimator), a slit (22 μm × 25 mm slit, metal film on glass), and a light source (Inframet LS-DAL). This light source combines two white LEDs and a 2856K halogen bulb in a mixed mode to achieve a consistent spectrum across the visible and near-infrared bands. To minimize external stray light, 3D-printed covers shield the setup's components.

The slit is mounted on a translation stage that rides on a 360-deg rotating stage with a central optical port. This configuration allows the slit to be scanned across the optical port in any direction. The setup lacks a hardware reference to indicate the scan center position where the slit intersects the rotation stage's axis. Instead, scans are repeated at an even number of angles around

Table 2 Parameters and camera settings used during measurements.

Parameter	HSI V4	HSI V6
Exposure time	240 ms	65 ms
Duration of measurement	28.8 h	6.5 h
Data set size	7.8 GB	2.8 GB

the full circle so that each LSF is recorded twice in opposing directions, enabling determination of the scan center.

Custom-made software controls the scan motion. The camera under test receives hardware trigger input from the motors, thereby syncing the data acquisition with the motor steps. The cameras are controlled by a separate software that captures data with predefined settings (exposure time, pixel clock) and without any preprocessing.

Initial tests were conducted to optimize the scan and camera settings (Table 2). The HSI V4, with its smaller optical components, gathers less light and thus requires a longer exposure time. This limitation reduces the frame rate, consequently extending the overall measurement time. In contrast, the HSI V6, benefiting from larger optics, can operate at shorter integration times, allowing for more rapid data collection.

For each camera 36 LSF, scans were recorded, with a 10-deg step between scans. The LSF scan length is chosen ~15 times longer than the pixel-to-pixel distance for both cameras. The LSF scans are oversampled to enable noise reduction by binning. The HSI V4 captured 12,000 images per LSF scan, whereas the HSI V6 recorded 10,000 images. Thus, each LSF recording has several hundred points within the nominal pixel width and extends well into the tails of the LSF for the neighborhood of pixels in the center of the scan area. Measurements were made at the center and the edge of the field of view (FOV) for each camera.

2.3 Data Analysis

The data processing approach follows the methodology described in Ref. 10. Initially, pairs of LSFs recorded in opposing directions are used to determine the scan center. This is achieved by reversing one of the datasets and finding the offset that maximizes the correlation between them. Once the offsets are applied, all LSFs are centered. To mitigate noise, groups of 10 frames are averaged, yielding 1000 and 1200 samples for each LSF after binning. Given that actual LSFs tend to be smooth due to diffraction blur, a Savitzky–Golay filter is applied to the binned LSFs to further reduce high-frequency noise.

The number of frames needed to cover one pixel during a scan is estimated from the number of frames between the LSF peaks of neighboring pixels. The average distance (in frames) between all the detected peaks serves as the conversion factor from frames to pixels in the subsequent plots.

Resolution and coregistration in the along-track and across-track directions are characterized using the LSFs in each direction. Typically, the resolution is quantified by the full width at half maximum (FWHM) of the LSF peak. In accordance with the P4001 draft, LSF peak width is here determined as the FWHM of a Gaussian having the same second moment as the measured LSF. The conventional keystone metric for spatial coregistration between bands in a pixel is expressed as the difference in centroid position between bands.

Finally, the full 2D SPSFs are reconstructed from the measured LSFs through tomographic reconstruction, as described in Refs. 9 and 11. This reconstruction uses the LSFs as 1D projections at various angles to build up a 2D image of the SPSF for each band. Noise can affect the results and is potentially amplified in the reconstruction process. (See Ref. 10 for more details on the exact reconstruction process used here.) The total enclosed energy is calculated as the integral of the SPSF over the image plane. To minimize residual noise, all values below a threshold corresponding to 5% of the total enclosed energy in the SPSF are removed. The resulting SPSFs for each band in a pixel enable evaluation of coregistration error between all band pairs. The 5% truncation threshold was set after an initial estimation of coregistration errors: As shown in Fig. 8, the cameras exhibit coregistration errors significantly larger than 5%; therefore, the

distortion of the results due to truncation of the SPSF is significantly smaller than the coregistration errors within the main part of the SPSF. For a camera with a lower level of coregistration error, the truncation threshold would have to be lower, possibly necessitating a longer total measurement time.

3 Results and Discussion

3.1 Spatial Resolution Across and Along Track

Examples of measured LSFs across and along track are shown in Fig. 2 for a set of wavelengths within the nominal spectral range of 400 to 800 nm for both HSI V4 and HSI V6. Measurements were taken from the center of the FOV for both imagers.

Figure 3 plots the FWHM along and across track for all bands as a function of wavelength. Sharp spikes in the plots occur because the LSF in those particular bands exhibits significant extra noise compared with neighboring bands. This noise caused the weighted second moment (variance) to be overestimated, resulting in a significantly larger FWHM for those bands.

The figure also shows the variation of raw signal level, integrated over the LSF. Signal levels are significantly reduced below 450 nm and above 650 nm due mainly to three factors: the anti-reflective coatings in the optical components are optimized for the visible spectral range, the diffraction efficiency is best for this spectral range, and focus across the spectral range is uneven. (The focus was optimized for shorter wavelengths.) In addition, the quantum efficiency of the image sensor is highest in the 450 to 650 nm range.

Significant variations in sharpness are observed in the across-track direction, clearly resulting from chromatic aberrations in the COTS objective lenses used. Structures in LSFs, such as the triple peak at 550 nm seen for V4 in the across-track direction, are also likely due to chromatic aberration. HSI V4 exhibits the sharpest focus at a wavelength of 450 nm, suggesting that the focus is optimized for shorter wavelengths. This is suboptimal for most applications, where focus
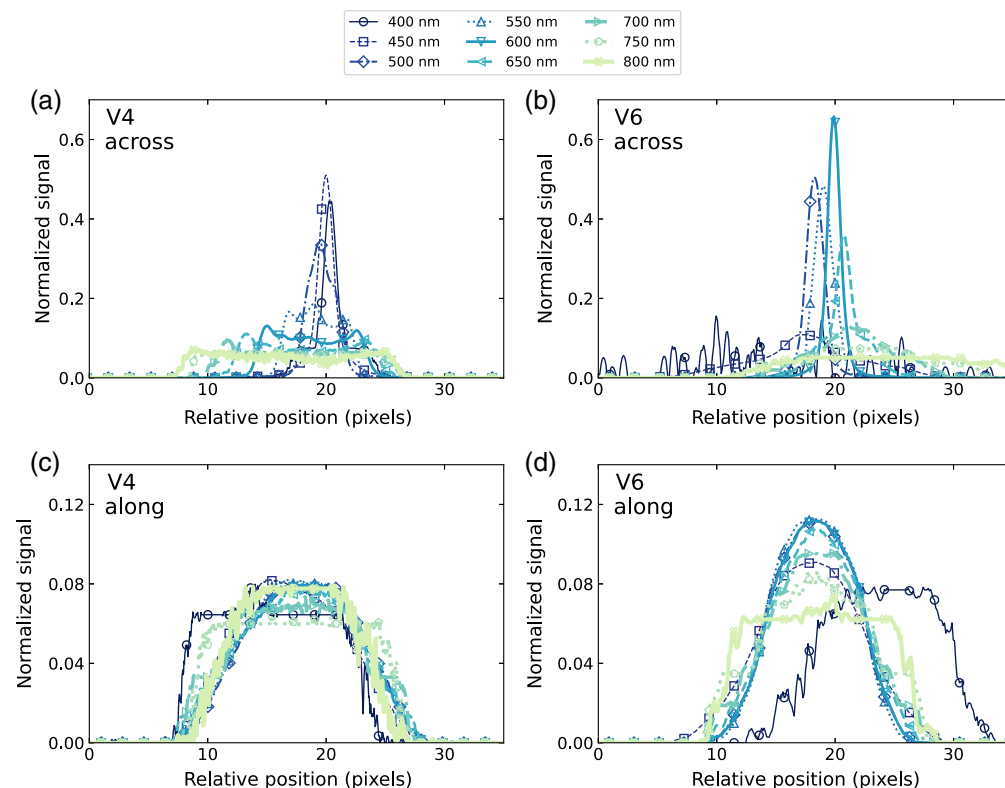

Fig. 2 LSFs for bands within the nominal spectral range for (a) HSI V4 across-track, (b) HSI V6 across-track, (c) HSI V4 along-track, and (d) HSI V6 along-track. LSFs are normalized to unit integral.
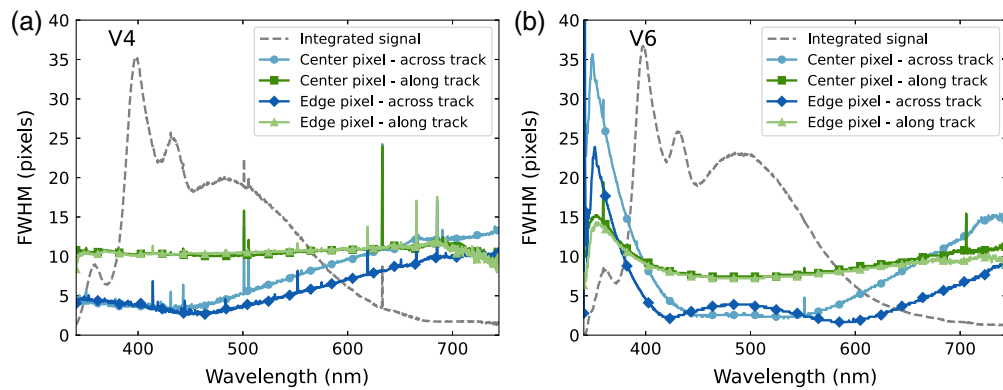
Fig. 3 Spatial resolution estimated for the along- and across-track direction for (a) HSI V4 and (b) HSI V6. Dashed gray line indicates relative variations in signal strength over the spectral range.

should ideally be best at the center wavelength. HSI V6, on the other hand, shows small variations in sharpness between ∼400 and 650 nm, with no features such as triple peaks observed.

For both instruments, the LSFs are significantly wider in the along-track direction. This is due to a design compromise where the slit width is chosen to be larger than the across-track pixel width, to collect more light, accepting some along-track blur as a tradeoff. Overall, the performance of HSI V6 varies less across track and is better in the along-track direction. Both cameras exhibit fair consistency in sharpness across the FOV.

A version of the HSI V6 is currently used on the HYPSO-1 cubesat.[12] The achieved spatial resolution from in-orbit was estimated in Ref. 13, where the FWHM of the across-track LSF was measured to be ∼2 to 3 pixels in the range of 450 to 750 nm. This is consistent with the observations for HSI V6 here.

3.2 Keystone Distortion

The keystone distortion is the across-track shift of the SPSF with wavelength. This distortion is shown for both cameras in Fig. 4, at the center and edge of the FOV. A nearly linear distortion is seen for the center pixel in both cases, with an amount comparable to the spectral response function peak width. This distortion is clearly due to a residual error in the rotational alignment of the image sensor relative to the diffraction grating because it is the orientation of the grating that determines the direction of the dispersion of light that is subsequently focused onto the image sensor. The edge pixels exhibit additional keystone error, particularly in the shortwave end of the spectrum, which appears to result from chromatic aberration in the lenses.

Previous measurements of keystone distortion for both HSI V4[14] and HSI V6[2] have shown similar patterns. In addition, the smile and keystone distortion for the version of HSI V6 used on HYPSO-1 were reported in Ref. 15. For HSI V4, keystone distortion was estimated to be ∼4 to 5
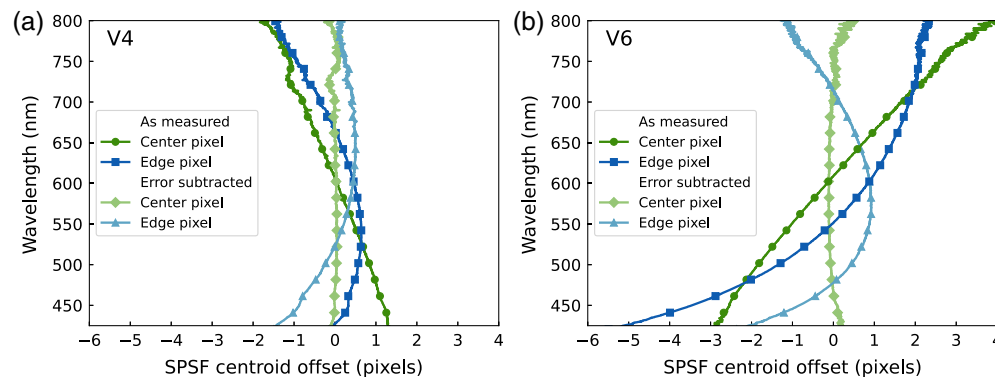

Fig. 4 Keystone for (a) HSI V4 and (b) HSI V6 as measured and after subtraction of the alignment error.

pixels in the 400 to 800 nm range. For HSI V6 in both Ref. 2 and HYPSO-1, the shift was found to be ∼2 pixels in the same spectral range. However, in our measurements, we observe a different pattern. This discrepancy is likely due to the use of different camera builds than those in Refs. 15 and 2, with varying calibration and alignment of the components.

3.3 Reconstructed 2D SPSFs

The full SPSFs reconstructed from the LSFs are shown for selected wavelengths in Figs. 5 and 6 for HSI V4 and HSI V6, respectively. Wavelengths between 450 and 650 nm were chosen due to the low signal-to-noise ratio outside this range.

For the HSI V4, the wavelength dependence reflects the behavior shown in Fig. 2, with the sharpest focus observed at the shortwave end. The elongation in the along-track direction results from the slit being wider along track than the pixel pitch across track. Significant defocus is seen at the longwave end. This is consistent with Fig. 2, but Fig. 5 shows that the SPSF broadening results from a complex shape of the 2D SPSF.
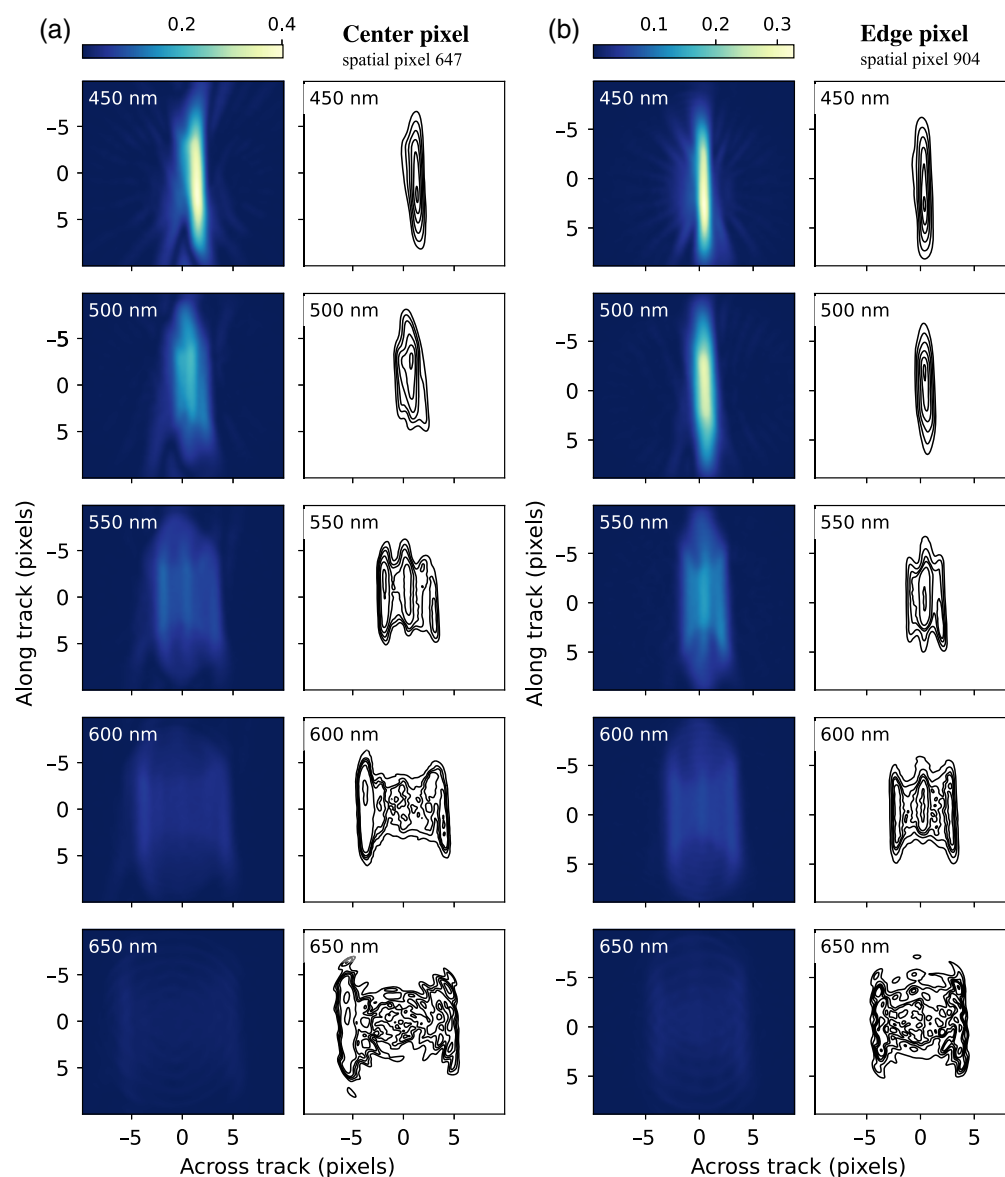

Fig. 5 Reconstructed SPSFs for HSI V4. The SPSFs for the center pixel (a) and the edge pixel (b). The contour lines indicate the levels at 50%, 60%, 70%, 80%, and 90% of the enclosed energy of the SPSF.

Fig. 6 Reconstructed SPSFs for HSI V6. The SPSFs for the center pixel (a) and the edge pixel (b). The contour lines indicate the levels at 50%, 60%, 70%, 80%, and 90% of the enclosed energy of the SPSF.
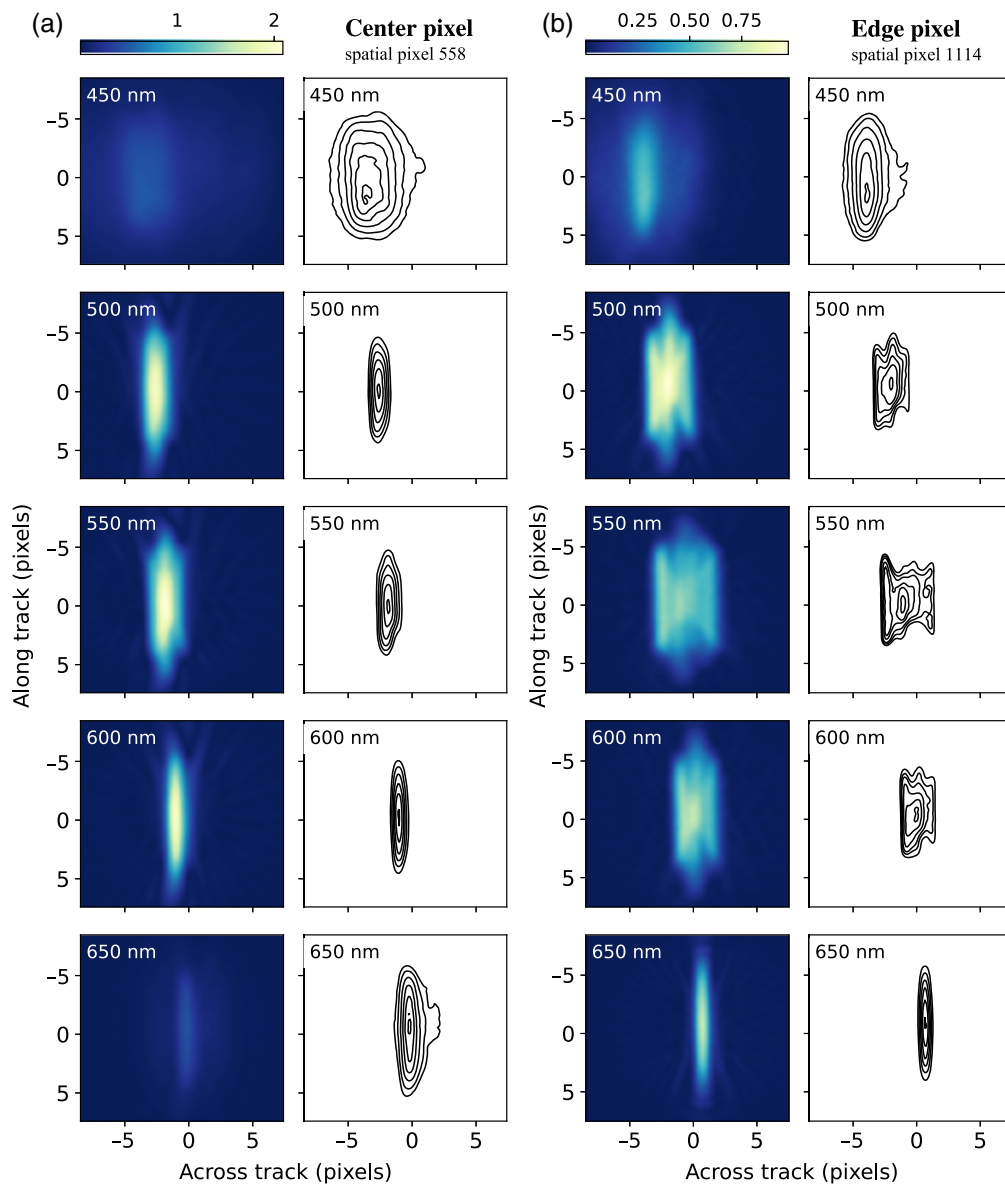
For HSI V6, focus is set so that the SPSF tends to broaden toward the ends of the spectral range. Generally, the SPSF is better focused than for HSI V4, which is consistent with the observations in Fig. 2. For HSI V6, the SPSF broadens differently than in HSI V4, with tails appearing in the SPSF at longer wavelengths.

In HSI V6, the opposite behavior is observed between the center and edge of the FOV, with smaller SPSFs found in the center. This is expected as better performance is typically observed in the center of the FOV, close to the optical axis.

3.4 Simplified Approximate SPSF Measurement

Recognizing that the tomographic 2D measurement is complex, the P4001 draft allows a simplified measurement of only two LSFs in orthogonal directions, deriving an approximate SPSF shape as the product of these, as discussed in Ref. 16. Thus, this simplified measurement assumes that the SPSF shape is well represented by such a separable function, which is not necessarily the case, but with the benefit of reduced measurement time and a simpler experimental setup similar to what many labs already have.
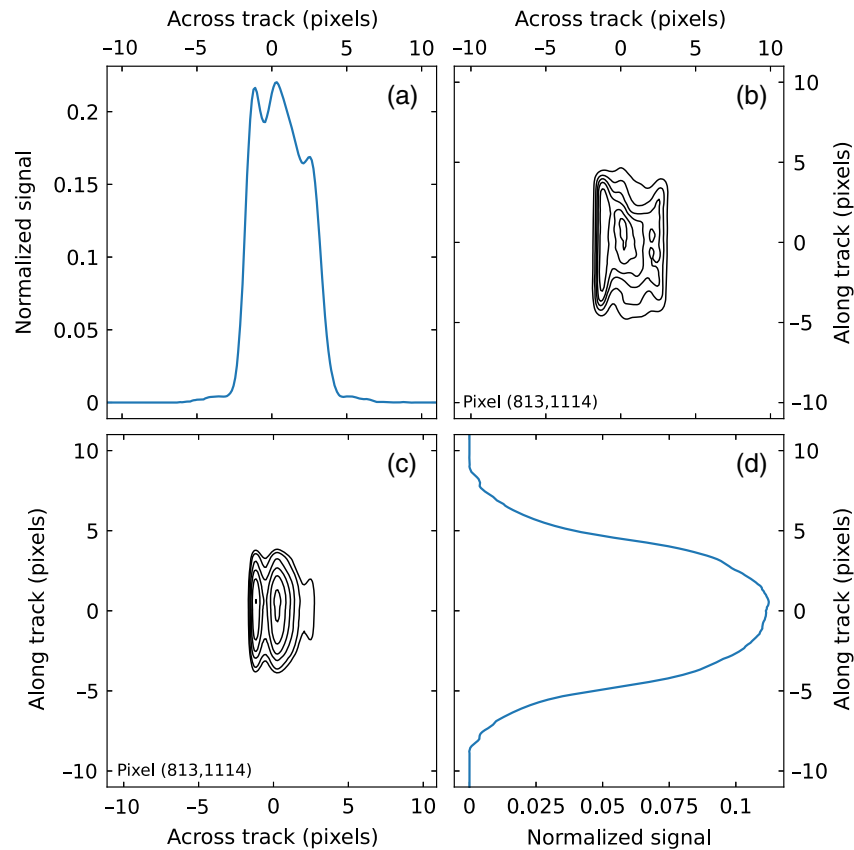
Fig. 7 Comparison of (b) fully reconstructed SPSF and (c) simplified SPSF for the HSI V6 edge pixel. Panels (a) and (d) show the LSFs in the across- and along-track directions, respectively.

As an example, Fig. 7 shows the fully reconstructed SPSF [panel (b)] for the 534 nm band of the HSI V6 edge pixel compared with the simplified SPSF [panel (c)] formed from the LSFs across and along track, shown in panels (a) and (d), respectively. The simplified SPSF in panel (c) is a fair representation of the full reconstructed shape in panel (b). The main features are retained, not least since the scan axes are chosen along the camera axes. Some asymmetry and skew is present in the full SPSF, but lost in the approximation. The full reconstructed shape appears broader in the contour plot, but this is partly because of a higher level of noise and reconstruction artifact in the SPSF tails, leading to contours being drawn at lower signal levels for a given enclosed energy.

3.5 Coregistration Error

Following the P4001 standard, we quantify coregistration as the integrated difference between SPSFs of two different bands in the same pixel:

$$\varepsilon_{xy} = \frac{1}{2} \iint_{x,y} |f_m(x,y) - f_n(x,y)| \mathrm{d}x\mathrm{d}y, \tag{1}$$

where x and y represent the coordinates of the image, and $f_m(x,y)$ and $f_n(x,y)$ are the SPSFs for bands m and n, normalized to unity integral. This quantity serves as an upper bound on the error in the reflectance that can be estimated from the image data.[8] Figure 8 shows the coregistration error matrix of Eq. (1) for all band pairs in both cameras, along with the average coregistration error. Panels (a) and (b) are matrices calculated from the fully reconstructed SPSFs, whereas panels (c) and (d) are based on simplified SPSF measurements.

As the matrix (1) is symmetric, we use the two halves in the figure to represent two different pixels: one at the center and one at the edge of the FOV. Unsurprisingly, SPSFs of neighboring bands are more similar and therefore exhibit less coregistration error than bands with larger spectral separation. In terms of the average coregistration error, the edge of the FOV for HSI V4
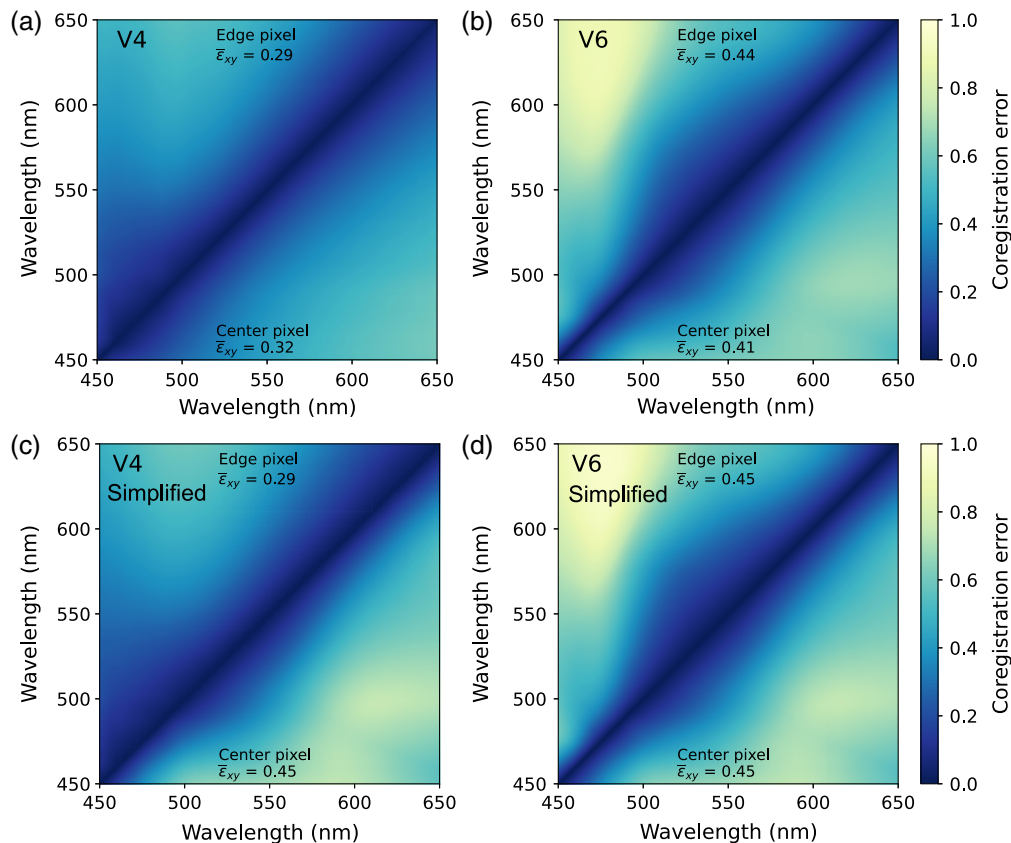
Fig. 8 Coregistration error matrices for (a) and (c) HSI V4, and (b) and (d) HSI V6. Matrices in panels (c) and (d) are derived from simplified SPSF measurements. The lower and upper halves are the coregistration error matrices for center and edge pixels, respectively. $\overline{\varepsilon}_{xy}$ is the average coregistration error.

shows the lowest error at 0.29, followed by the center of the FOV for HSI V4 at 0.32, the center of the FOV for HSI V6 at 0.41, and finally the edge of the FOV for HSI V6 at 0.44. This pattern is consistent with the SPSF plots (Figs. 5 and 6). The simplified measurement gives a slightly larger coregistration error for V6 but overestimates more significantly the error value for the center pixel of V4. Looking back at Fig. 5, the SPSF for this pixel is severely distorted. In terms of use in camera characterization, it can be seen as a good thing that the simplified measurement provides a conservative value.

Notably, although HSI V6 exhibits an overall sharper SPSF, it also has the highest coregistration error. This is evident in Fig. 6, where the sharp SPSF at 650 nm overlaps very little with the SPSF at 450 nm. This misalignment is due to a combination of keystone distortion and SPSF broadening at the blue end of the spectral range. If the observed scene is not uniform around the pixel, this will clearly distort the observed spectrum. For example, consider a pixel region with a vertical edge at $x = 0$ in Fig. 5 or 6, with a white area on the left and a black (or shadow) area on the right. The 450-nm band will predominantly see white, whereas the 650-nm band will predominantly see black. Thus, the measured spectrum will be severely distorted.

4 Conclusions

We have performed an extensive characterization of the spatial characteristics of two hyperspectral cameras with nominally similar performance, built from different sets of COTS components. Through measurement of the full SPSF shape, we have characterized spatial resolution, coregistration error, and residual alignment errors. The results clearly indicate residual errors in the focusing and alignment of HSI V4. In addition, the COTS objective lenses used impose limitations on sharpness and coregistration, even though these lenses, particularly those used in V6, are considered high quality for conventional imaging.

Although spectral properties were not part of the testing here, it appears likely that the low signal-to-noise ratio outside the visible spectral range is at least partly due to losses in antireflection coatings optimized for the visible spectrum. Generally, it is unsurprising that the performance of the two cameras is limited when using COTS lenses in applications for which they are not optimized. An interesting finding is that the coregistration error is larger for the V6 camera, which exhibits better sharpness. Thus, when imaging a remote sensing scene with strong contrasts (e.g., shadows) on all spatial scales, the integrity of the measured spectra will be better for HSI V4 than for HSI V6. Coregistration can be improved by spatial binning, which involves a tradeoff against spatial resolution.

Having detailed information about the SPSF shape can be helpful in optimizing the binning scheme according to specific application requirements. Another possibility enabled by the 2D mapping of SPSFs that warrants further study is to use the measured SPSFs to create an optimized resampling scheme. This approach could result in images with an optimized combination of resolution and coregistration according to the requirements of a given application. Overall, the COTS-based hyperspectral cameras have the potential to produce useful hyperspectral imagery in cost-sensitive applications where lower spatial resolution is acceptable.

At present, the body of published SPSF measurements on hyperspectral cameras is very limited. Compared with previous results from a high-end camera in Ref. 9, the results here are examples of cameras at the opposite end of the performance scale. Also, the simplified SPSF measurement method has been shown to produce reasonable results for the cameras under test. Our methods and results will hopefully be a useful point of reference when setting up camera characterization for the upcoming IEEE P4001 standard.

Disclosures

The authors declare no conflicts of interest.

Code and Data Availability

Data and code used in this work are available upon request.

Acknowledgments

References

1. F. Sigernes et al., "Do it yourself hyperspectral imager for handheld to airborne operations," *Opt. Express* **26**(5), 6021–6035 (2018).
2. M. B. Henriksen et al., "Do-it-yourself VIS/NIR pushbroom hyperspectral imager with C-mount optics," *Opt. Continuum* **1**(2), 427 (2022).
3. E. F. Prentice et al., "Design of a hyperspectral imager using COTS optics for small satellite applications," in *Int. Conf. Space Optics - ICSO 2020*, SPIE (2021).
4. J. R. Gilchrist, T. Skauli, and C. Durell, "Developing the IEEE P4001 standard for characterisation and calibration of hyperspectral imaging devices," in *IGARSS 2022-2022 IEEE Int. Geosci. Rem. Sens. Symp.*, pp. 4679–4682 (2022).
5. A. Baumgartner et al., "Characterisation methods for the hyperspectral sensor hyspex at DLR'S calibration home base," *Proc. SPIE* **8533**, (2012).
6. P. Gege et al., "Calibration facility for airborne imaging spectrometers," *ISPRS J. Photogramm. Rem. Sens.* **64**, 387–397 (2009).
7. J. Fisher et al., "Comparison of low-cost hyperspectral sensors," *Proc. SPIE* **3438**, (1998).
8. T. Skauli, "An upper-bound metric for characterizing spectral and spatial coregistration errors in spectral imaging," *Opt. Express* **20**(2), 918–933 (2012).

9. H. E. Torkildsen and T. Skauli, "Full characterization of spatial coregistration errors and spatial resolution in spectral imagers," *Opt. Lett.* **43**(16), 3814–3817 (2018).

10. G. M. Selnesaunet, M. B. Henriksen, and T. Skauli, "Imaging the point spread function of hyperspectral cameras: the full truth about coregistration error and resolution," *Proc. SPIE* **12688**, 1268804 (2023).

11. H. Hovland, "Tomographic scanning imager," *Opt. Express* **17**(14), 11371 (2009).

12. M. E. Grøtte et al., "Ocean color hyperspectral remote sensing with high resolution and low latency: the HYPSO-1 CubeSat mission," *IEEE Trans. Geosci. Rem. Sens.* **60**, 1000619 (2021).

13 S. Bakken et al., "HYPSO-1 CubeSat: first images and in-orbit characterization," *Rem. Sens.* **15**(3), 755 (2023).

14. M. B. Henriksen et al., "Real-time corrections for a low-cost hyperspectral instrument," in *10th Workshop Hyperspectral Image Signal Processing, Evolution in Remote Sensing (WHISPERS)*, IEEE Xplore (2019).

15. M. B. Henriksen et al., "Pre-launch calibration of the HYPSO-1 cubesat hyperspectral imager," in *IEEE Aerospace Conf.* (2022).

16. T. Skauli and H. E. Torkildsen, "Simplified measurement of point spread functions of hyperspectral cameras for assessment of spatial coregistration," *Proc. SPIE* **10986**, 109860E (2019).

Gard Momrak Selnesaunet is a PhD research fellow at the Center for Space Systems and Sensors (CENSSS), Department of Technology Systems, University of Oslo (UiO). His research focuses on the characterization of hyperspectral imagers and other types of cameras. He obtained his master's degree from UiO, where he focused on fabricating opto-electric nanostructures and material characterization using a scanning electron microscope and cathodoluminescence.

Marie Bøe Henriksen received her PhD from the Department of Engineering Cybernetics, Norwegian University of Science and Technology (NTNU) in 2023, where she focused on the calibration and characterization of hyperspectral imagers used in the HYPSO cubesat mission.

Torbjørn Skauli is a professor of optical sensors at the University of Oslo, Department of Technology Systems. His work involves various imaging techniques for terrestrial and space applications, including methods and metrics for camera characterization. He is currently vice chair of the IEEE P4001 standard development group.